

# Atomistic Structures of 25 000-Atom Oxide Nanoparticles Supported on an Oxide Substrate

Dean C. Sayle<sup>\*,†</sup> and Graeme W. Watson<sup>‡</sup>

*Department of Environmental and Ordnance Systems, Cranfield University, Royal Military College of Science, Shrivenham, Swindon, U.K. SN6 8LA, and Department of Chemistry, Trinity College, Dublin 2, Ireland*

Received: May 30, 2002; In Final Form: July 27, 2002

A simulated amorphization and recrystallization strategy has been used to generate atomistic models of CaO and SrO nanoparticles, approximately  $13 \times 13 \times 3$  nm in size, supported on an MgO(001) substrate. The (single crystal) CaO nanoparticle exhibits a cubic “slab” morphology in contrast to the SrO nanoparticle, which has a convex-lens or “droplet” morphological appearance with a height of 3.5 nm and a diameter of about 14–15 nm. In addition, the SrO nanoparticle comprises 10 interconnecting misoriented crystallites. The epitaxial relationships that exist between the nanoparticle and substrate are identified and correlated with the lattice misfit together with the interfacial structures and complex dislocation networks that evolve within the nanoparticles. The atomistic structure of various screw-edge dislocation cores (in CaO), grain-boundaries, and grain-junctions (in SrO) that form within the nanoparticles are presented graphically. In addition, the structures of the nanoparticles are compared with previous simulations performed on the analogous CaO and SrO thin films supported on MgO(001).

## Introduction

When an oxide thin film is supported on a lattice misfitting oxide substrate, the overlying oxide evolves various structural features to maximize the interfacial interactions, while minimizing the strain associated with the incommensurate nature of the system. These structural modifications may include grain-boundaries,<sup>1,2</sup> dislocation arrays,<sup>3–5</sup> lattice slip<sup>6</sup> defects including vacancies, interstitials, and substitutionals, and defect clustering particularly at the interfacial region,<sup>7</sup> where there is likely to be a reduction in the ionic density.<sup>8</sup> These structural features influence considerably the chemical, physical, and mechanical properties of a material. Consequently, in designing devices, which comprise thin films, such as supported catalysts,<sup>9</sup> superconductors,<sup>10</sup> sensors<sup>11</sup> and recording media,<sup>12</sup> it is desirable to understand the nature of these structural features and the corresponding changes in material properties they give rise to. Ultimately, one requires the ability to tailor such structural features in order that the material properties are optimized for the particular application.

A further area of intense research, similar to that of supported thin films, is clusters and nanoparticles.<sup>1,13</sup> In particular, as the size of the material reduces to the nanometer scale, the properties change uniquely in comparison with the bulk characteristics of the parent material.<sup>14</sup> The origins of which may be attributed to the dimensions of the particles being comparable to the length scales of basic quanta in solids (phonon wavelengths, de Broglie wavelengths of electrons). Moreover, because most of the ions comprising the material are located at surface or near-surface regions, surface effects dominate the thermodynamics and energetics of the particle (crystal structure, morphology, reactivity, etc). If one then were to support a nanoparticle on a lattice misfitting substrate, further structural modifications will arise.

Here, we aim to explore the influence of the substrate on the morphological and structural features of supported oxide nanoparticles, using atomistic simulation techniques.

The area of nanoscience has recently enjoyed explosive growth, which can perhaps be attributed to two primary reasons: first, to exploit the remarkable properties of such materials (together with the envisaged plethora of associated applications) and, second, methods of controllable nanoparticle synthesis are now available (for example see ref 12). However, experimental elucidation of the complete three-dimensional atomistic structure of such systems, which include, for example, dislocations and grain-boundaries, is difficult.<sup>7,15</sup> Although there has been much effort directed at metal clusters and nanoparticles supported on an oxide substrate,<sup>13</sup> there is less data pertaining to oxide nanoparticles supported on oxide substrates<sup>16</sup> because of the problems associated with the insulating nature of many oxide materials.<sup>7</sup> Accordingly, in this study, atomistic simulation techniques are used to generate models of supported oxide nanoparticles. In particular, atomistic simulation has been employed in a predictive capacity to explore how structural modifications induced within the supported oxide are related to the underlying substrate and the associated lattice misfit of the system. Indeed, with the increase in speed of modern computers, all of the ions comprising the nanoparticle can be treated explicitly without resorting to continuum methods.

Atomistic simulation appears at first sight an ideal approach with which to explore such features. For example, one might expect that when an oxide is placed on top of an oxide substrate all of the structural features will evolve as dynamical simulation or energy minimization directs the ions into low energy configurations. However, within crystalline oxide materials, because the energy barriers for ionic migration are high, the time scales accessible to dynamical simulation (typically nanoseconds) are insufficient to enable such structures to evolve. Similarly, for energy minimization, the simulation is likely to

\* To whom correspondence should be addressed. E-mail: sayle@rmcs.cranfield.ac.uk.

† Cranfield University.

‡ Trinity College.

simply find the nearest local energy minima, which may be of high energy and highly dependent upon the starting configuration.

One suggestion therefore might be to increase the temperature and so increase the ionic mobility. At the limit, this would involve melting the oxide thin film and then slowly cooling and recrystallizing the material; within a molten material, the mobility of ions is considerable compared with the analogous solid,<sup>17</sup> and within the time scales accessible, the increased ionic mobility would allow the ions to move into low energy configurations. Here, we adopt a similar scenario. However, rather than melt the thin film, we force the overlying material to undergo a controlled amorphization. For an amorphous material, the activation energy barriers associated with ions moving through the lattice are much lower compared with those of crystalline material. This is because the ions do not lie in a deep energy well as they would within a crystalline material; rather, as they move within the amorphous solid, they experience a much shallower potential. The ionic mobility is therefore increased considerably and is analogous to the mobility within a molten material, enabling the ions to rearrange significantly within the limited time scales accessible to dynamical simulations. To induce amorphization, the overlying material is constrained under considerable tensile or compressive strain; the subsequent application of dynamical simulation to the system induces an amorphous (solid) transition. The prolonged application of dynamical simulation at reduced temperatures enables the oxide to recrystallize. Moreover, the ions will evolve naturally all of the structural features one would expect within an interfacial system<sup>6,7,15</sup>. In contrast to many previous studies, this amorphization and recrystallization strategy allows various structural features together with epitaxial configurations to evolve naturally in response to the lattice misfit and interactions from the underlying substrate. Accordingly, the introduction of structural features such as dislocations, grain-boundaries, and defects "by-hand"<sup>18,19</sup> together with geometrically arranging the two interfaced lattices to generate low-misfit epitaxial configurations<sup>20</sup> are no longer necessary. In addition, because the overlying thin film is forced to undergo an amorphous transition, all memory of the (perhaps artificial) preparative configuration is eliminated.

The procedure has thus far been applied to thin films including rocksalt structured oxides supported on oxide supports with associated high positive lattice misfits, BaO/MgO(001) ( $F = +27\%$ ); SrO/MgO(001) ( $F = +21\%$ ); CaO/MgO(001) ( $F = +13\%$ ),<sup>6</sup> and high negative lattice misfits, MgO/BaO-(001) ( $F = -27\%$ ),<sup>2,21</sup> perovskite structured substrates MO/SrTiO<sub>3</sub>(001) (M = Mg, Ba),<sup>22</sup> and fluorite structured materials CeO<sub>2</sub>/YSZ(001),<sup>23</sup> the latter are important components of exhaust catalysts. The lattice misfit of the system,  $F$ , is given by

$$F = \frac{2(a_1 - a_2)}{a_1 + a_2} \quad (1)$$

where  $a_1$  is the lattice parameter of the supported nanoparticle or thin film and  $a_2$  is the lattice parameter of the substrate. Accordingly, the calculated misfits are +13% for the CaO/MgO-(001) system and +21% for SrO/MgO(001); the lattice parameters of CaO, SrO, and MgO are 4.80, 5.16, and 4.20 Å respectively.

In previous studies, periodic boundary conditions (PBC) were required to model thin films, which can have significant limitations for supported thin films. In particular, the overlying oxide is continuous through the boundary, and for small

simulation cell sizes, only certain epitaxial configurations are possible.<sup>20</sup> A near coincidence site lattice model<sup>24</sup> can be used to determine geometrically the configurations with low associated misfit.<sup>20</sup> For example, if one were to consider the SrO/MgO(001) system, a good match might involve 9 repeat units of the overlying SrO with 11 repeat units of the underlying MgO substrate. Consequently, if the simulation (with PBC) were designed with a substrate 11 × 11 in area (along the [100] and [010]), the thin film may evolve to give this 9 × 9 lattice matched with 11 × 11 of the substrate. Here, the misfit is given by

$$F = \frac{2(ma_1 - na_2)}{ma_1 + na_2} \quad (2)$$

where  $m$  and  $n$  represent the epitaxial matching. In this case, the misfit would be 0.5%;  $m = 9$ ,  $n = 11$ . To accommodate perfectly this commensurate configuration and bring the lattices into coincidence,<sup>24</sup> the SrO thin film must be compressed,  $C$ , by +0.5% following

$$C = \frac{9a_{\text{SrO}} - 11a_{\text{MgO}}}{9a_{\text{SrO}}} \quad (3)$$

However, if the substrate were smaller, i.e., 10 × 10, this configuration would no longer be possible. One solution to this problem is to increase the size of the simulation cell. This enables a variety of configurations to exist within a single cell<sup>25</sup> and facilitates the evolution of dislocations within the thin film,<sup>5</sup> which accommodates, in part, any residual strain owing to the geometrical configurations.<sup>26</sup> However, it is unclear at present how large the interfacial area of the simulation cell should be to ensure convergence.<sup>5,27</sup> Conversely, for a supported nanoparticle the overlying oxide can evolve any low-energy configuration without being constrained to ensure continuity between neighboring (image) cells. The only limitation is the strength of the *interactions* between neighboring images. However, in this present study, the distances between a nanoparticle and its periodic images are sufficiently large (approximately 60 Å) to ensure that these interactions are negligible. Clearly, the influence of imposing PBC to study supported nanoparticles is less severe in comparison to thin films, which completely cover the surface.

In a previous study, we explored, using a simulated amorphization and recrystallization strategy,<sup>5,25</sup> the structures of oxide nanoparticles supported on an oxide, which has a higher lattice parameter.<sup>21,28</sup> Specifically, MgO, CaO, and SrO supported on BaO(001) or systems associated with a large *negative* lattice misfit. Here, we extend this previous study to include CaO and SrO nanoparticles and thin films supported on MgO(001), which are systems associated with a large *positive* misfit.

## Methodology

In this section, the potential models used in the study are presented, together with a description of the simulation code followed by a discussion of the amorphization and recrystallization strategy employed to generate models for the nanoparticles and thin films.

**Potential Models.** The reliability and quality of the simulations presented here are critically dependent upon the potential models used to describe the interactions between ions comprising the materials under investigation. The interionic potential models used in the study are, as is common for metal oxides, based upon the Born model of the ionic solid in which the ions interact via long-range Coulombic interactions and short-range

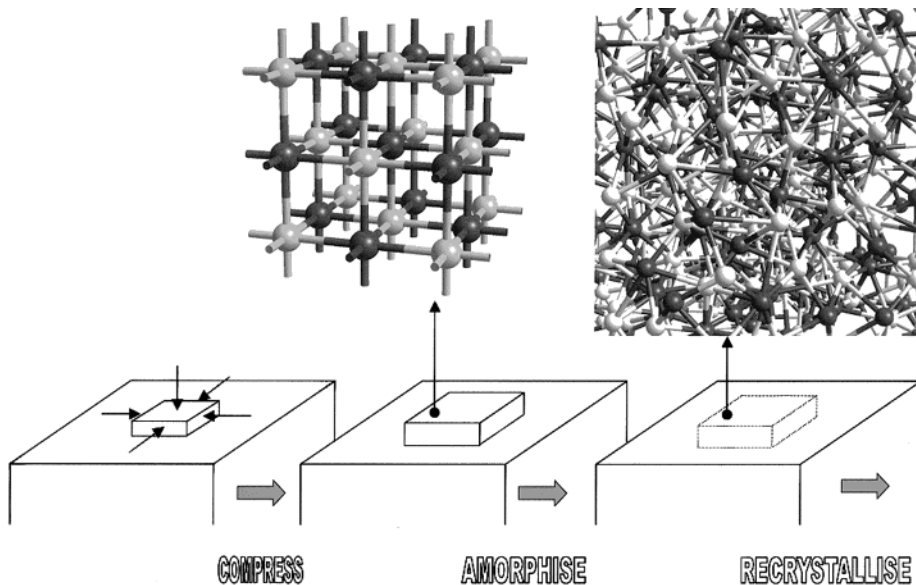


**Figure 1.** Schematic illustrating the amorphization and recrystallization strategy as applied to the generation of supported nanoparticles. A nanoparticle of SrO is placed on an MgO(001) substrate and compressed; a small segment of the MgO nanoparticle is depicted illustrating the rocksalt structure of the material at this stage. Upon the application of dynamical simulation, performed at high temperature, the considerable (compression induced) strain within the SrO lattice results in the amorphization of the nanoparticle. Again a small segment of the nanoparticle is depicted to show the amorphous structure. Finally, upon prolonged dynamical simulation, the amorphous SrO nanoparticle recrystallizes.

parametrized interactions. In this study, we have employed the potentials of Lewis and Catlow,<sup>29</sup> with the additional approximation of the rigid ion model, imposed to reduce considerably the computational expense. Because the amorphization and recrystallization technique requires the potential to describe the energy functional between two interacting ions over a considerable range of distances, the potential model must be robust and reproduce structures with nonoptimal geometries. The potential parameters of Lewis and Catlow have been extensively employed and tested previously<sup>5</sup> showing good correlation to experiment.<sup>15</sup>

**Simulation Codes.** The DL\_POLY code<sup>30</sup> is used in this study to perform all the dynamical simulations. Because this code utilizes three-dimensional periodic boundary conditions, the surface of the MgO substrate is simulated using a periodic array of slabs with a void introduced, perpendicular to the interfacial plane to represent the vacuum above the surface of the thin film. The size of the void is, of course, suitably large to ensure that the interactions between slabs are negligible.

In addition, a standard two-region approach<sup>31</sup> is employed: Region I contains the CaO or SrO nanoparticle and one repeat unit (two MgO(002) lattice planes) of the underlying MgO support and ions within this region are allowed to move within the dynamical simulation. Conversely, the ions in region II, which comprises three MgO repeat units thick (six MgO(002) layers), are held fixed to reproduce the potential of the bulk lattice on region I.

**Generation of Nanoparticles.** To generate models for the CaO and SrO nanoparticles supported on an MgO(001) substrate, we have employed a simulated amorphization and recrystallization strategy. A MO nanoparticle ( $M = \text{Ca}, \text{Sr}$ ) comprising 25 088 atoms and exposing {001} planes at each of the six surfaces,  $56 \times 56$  atoms in area and 8 atoms high was placed on the surface of an MgO(001) substrate. The surface of the MgO(001) substrate was  $84 \times 84$  atoms (176.8 Å in [100] and [010]) giving a surface area of approximately 31 000 Å<sup>2</sup>.

For the SrO/MgO system, the SrO nanoparticle was compressed by 43% and dynamical simulation performed at 2000 K for 0.5 ps. This procedure resulted in the formation of an

amorphous SrO nanoparticle. Essentially, the simulation involved compression-induced amorphization. Dynamical simulation was then performed on the system: 100 ps at 20 K, 380 ps at 50 K, 5 ps at 200 K, 120 ps at 400 K, 145 ps at 1500 K, 15 ps at 1000 K, 85 ps at 500 K, and finally 25 ps at 0 K. The latter acts effectively as an energy minimization. A schematic illustrating the procedure is presented in Figure 1.

For the CaO/MgO system, the CaO nanoparticle was compressed by 34%, and dynamical simulation was performed at 2000 K for 0.5 ps resulting in the formation of an amorphous CaO nanoparticle. Dynamical simulation was then continued: 90 ps at 20 K, 5 ps at 400 K, 225 ps at 1500 K, 5 ps at 1000 K, 5 ps at 500 K, and finally, 215 ps at 0 K.

The 43 and 34% compressions for SrO and CaO are somewhat higher than was employed previously to model thin films.<sup>26</sup> This was required to ensure complete amorphization of the clusters. The initial compression of the nanoparticles can be relieved (which ultimately leads to the amorphous transition), under dynamical simulation via expansion of the nanoparticle in directions both perpendicular and parallel with the interfacial plane. Preliminary tests revealed that smaller compressions resulted in the sides of the nanoparticle retaining the crystalline structure of the preparatory configurations. The supported thin films are more constrained as strain relief is facilitated only by expansion normal to the interfacial plane,<sup>5</sup> and therefore, amorphization can be achieved with smaller initial compressions of the overlying oxide.

In addition, once an amorphous nanoparticle had been generated, the temperature of the dynamical simulation was reduced to 20 K. Preliminary tests showed that if dynamical simulation were continued at high temperature immediately after amorphization had been induced, owing to the enormous compressive strain within the system, the nanoparticle spread completely over the surface of the MgO substrate resulting in a thin film as opposed to the desired nanoparticle. Accordingly, performing dynamical simulation on the system at low-temperature enabled the strain within the lattice to be quenched without resulting in complete spreading of the nanoparticle. After which dynamical simulation at higher temperature could be applied

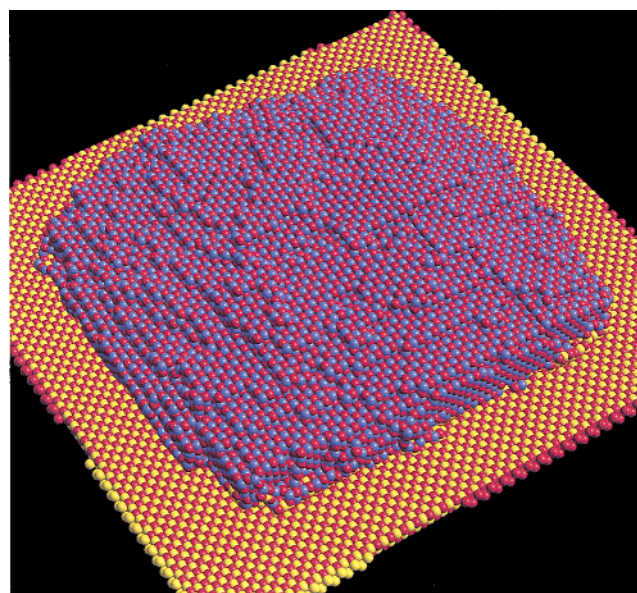


**Figure 2.** Sphere model representation with perspective of the atom positions for the CaO nanoparticle supported on an MgO(001) substrate. For reasons of clarity, only two MgO(002) planes are shown. Calcium ions are colored blue, magnesium is yellow, and oxygen is red.

to the (still amorphous) system, which comprised little compressive strain. Clearly, recrystallization could have been achieved by continuing the dynamical simulation at 20 K. However, the ionic mobility is low at this temperature, and therefore, the duration of the dynamical simulation would have exceeded computational resources. For a previous study on MgO, CaO, and SrO nanoparticles supported on BaO(001), the intermediate step of performing dynamical simulation on the system at low temperatures was not required because amorphization was induced via tension.<sup>28</sup> The procedures employed for generating the analogous CaO and SrO thin films supported on an MgO(001) substrate have been reported previously.<sup>6</sup>

It is also reasonable to correlate this simulated amorphization and recrystallization with recrystallization, which exists for real systems such as vapor deposition. However, the amorphous transition is facilitated by introducing considerable compressive or tensile stresses within the overlying material. Consequently, the initial amorphous configurations are of high energy, and velocity scaling of the ions to the simulation temperature must be imposed throughout the simulation. The structural evolution of the nanoparticle or thin film bears little physical significance, and therefore, the procedure cannot be likened to recrystallization, which occurs for real systems. Rather, the simulation is a technique for deriving a range of low energy configurations comprising various structural features, which are observed in real systems, and it is only the final structures that are useful models that can be compared with experiment.

## Results

To understand the structures of the resulting supported nanoparticles and thin films, graphical techniques are employed to examine the morphological appearance of the systems, the structures of the interfacial regions, epitaxial configurations that evolve together with various structural features, such as grain-boundaries, dislocation networks and defects.

**Morphologies. *CaO/MgO(001)*.** Inspection of the atom positions of the CaO nanoparticle, presented in Figure 2, reveals a cubic slab morphological appearance with a size of about  $127 \times 133 \times 30$  Å. The nanoparticle comprises a single crystal exposing predominantly {001} facets. These facets include many

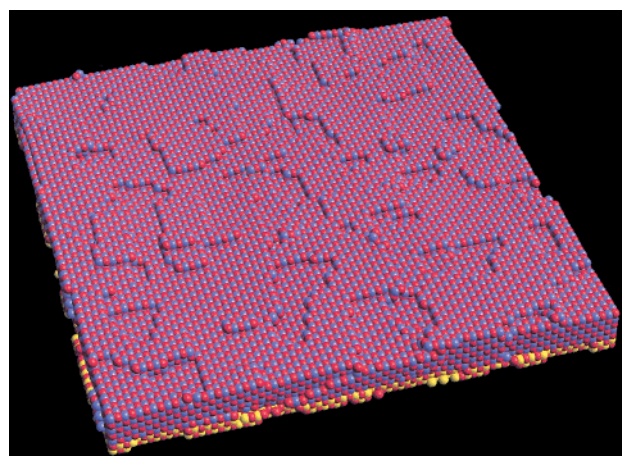


**Figure 3.** Sphere model representation with perspective of the atom positions for the CaO thin film supported on an MgO(001) substrate. For reasons of clarity, only two MgO(002) planes are shown. Calcium ions are colored blue, magnesium is yellow, and oxygen is red.

monatomic and, occasional, diatomic steps on the surface, traversing down from the center (highest point) of the nanoparticle to the edges, which give rise to an almost lens-type morphology. The nanoparticle appears to lie with CaO(001) planes parallel with the (001) plane of the underlying support albeit the CaO(001) planes exhibit some curvature, which contributes further to the lens-type morphological appearance of the nanoparticle. In comparison, the analogous CaO/MgO(001) thin-film system (Figure 3) exposes the {001} surface at the interface and surface of the thin film with predominantly monatomic and occasionally diatomic steps on the surface of the CaO. We also note that neither the nanoparticle nor the thin film are rotated about an axis perpendicular to the interfacial plane. For example, in a previous study<sup>22</sup> of BaO supported on SrTiO<sub>3</sub>, the BaO rotated by 45° about an axis perpendicular to the interfacial plane, resulting in a reduction of the lattice misfit from +34% to -0.3%. Similar rotations of oxides on a substrate have been reported experimentally.<sup>7</sup>

**SrO/MgO(001).** Inspection of the atom positions of the SrO nanoparticle, presented in Figure 4a,b, reveal broadly that the nanoparticle exhibits a convex lens-type (“droplet”) morphological appearance. A plan view of the system reveals the nanoparticle to be almost circular with a diameter of about 145 Å. In contrast to the CaO nanoparticle, which appears as a single crystal, the SrO nanoparticle comprises 10 misoriented crystallites, which intersect resulting in the formation of grain boundaries and grain junctions. The orientational relationships of the various crystallites with respect to the underlying MgO(001) substrate are complex and difficult to assign. Moreover, the [001] of the various crystallites comprising the nanoparticle do not lie parallel with the [001] of the substrate; rather they subtend various angles. Although many of the angles are small, suggesting vicinal SrO(001)/MgO(001), certain grains subtend a much larger angle (Figure 4c), which gives rise, in part, to the droplet morphological appearance of the nanoparticle. In addition, inspection of a plan view of the system, Figure 4a, reveals that certain crystallites are rotated by various angles (up to 45°), about the [001], with respect to the underlying substrate.

Each crystallite exhibits, at the surface, predominantly {001} facets with many monatomic and, occasionally, diatomic steps, which traverse down from the central (highest) point of the nanoparticle to the edges, resulting in a more spherical (lens-type) morphological appearance to the structure of the nanoparticle.

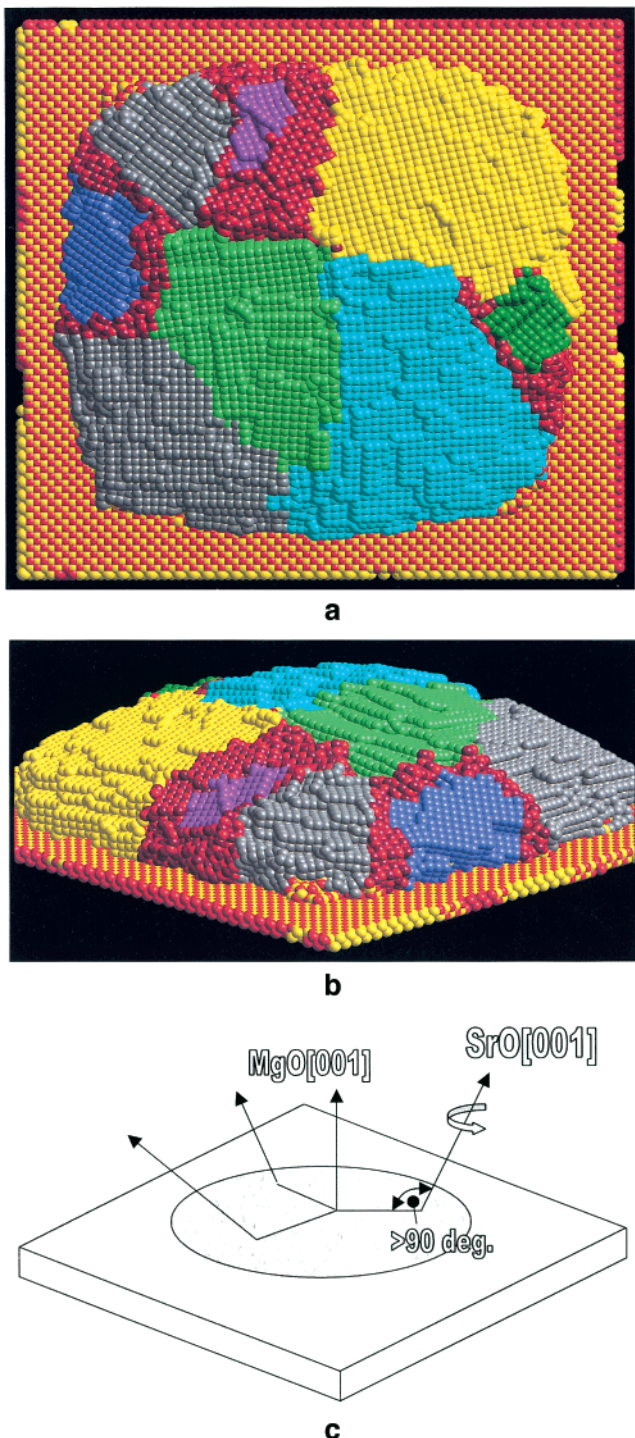


**Figure 4.** Sphere model representation of the atom positions for the SrO nanoparticle supported on an MgO(001) substrate; (a) plan view; (b) side view with perspective showing the lens type morphological appearance of the nanoparticle; (c) schematic illustrating the various orientations of SrO(001) planes terminating at the surface of the nanoparticle with respect to the interfacial plane and which contribute to the lens-type morphological appearance of the nanoparticle. Only two MgO(002) layers of the underlying substrate are depicted to ensure clarity of the figure. For the substrate, magnesium ions are colored yellow and oxygen ions are red, whereas the various misoriented crystallites comprising the SrO nanoparticle are colored to aid visualization.

In comparison to the lens-type morphology of the cluster, the SrO thin film completely covers the surface exposing {001} surfaces at the surface and interface (Figure 5). Similar to the CaO thin-film system, monatomic and occasionally diatomic

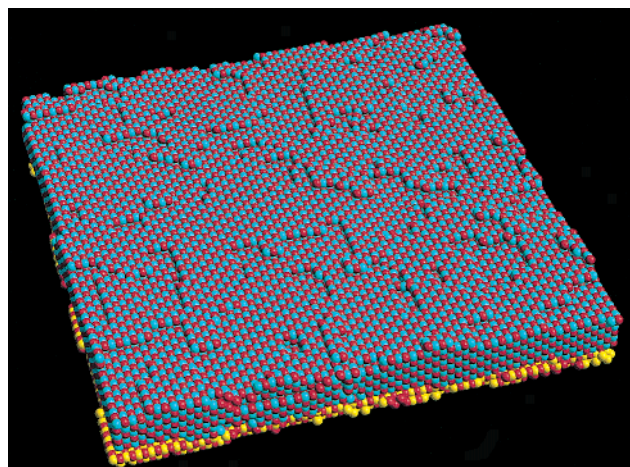


**Figure 5.** Sphere model representation with perspective of the atom positions for the SrO thin film supported on an MgO(001) substrate. For reasons of clarity, only two MgO(002) planes are shown. Strontium ions are colored light blue, magnesium is yellow, and oxygen is red.

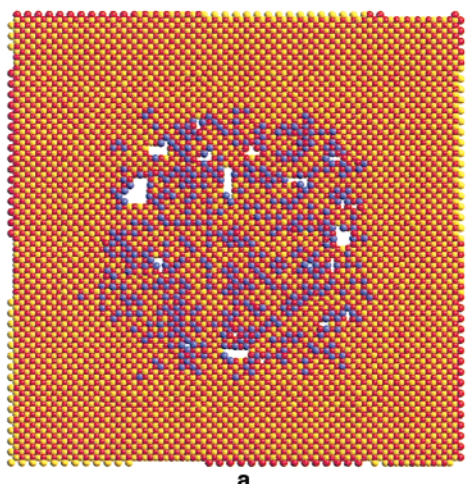
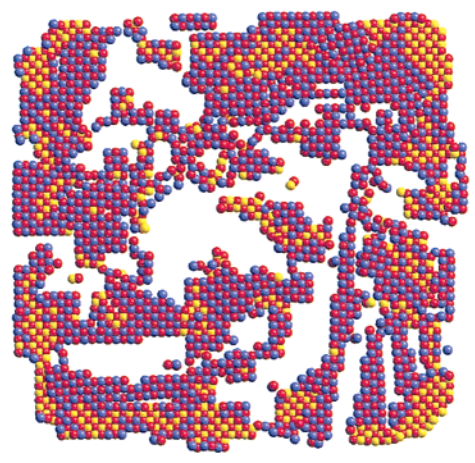
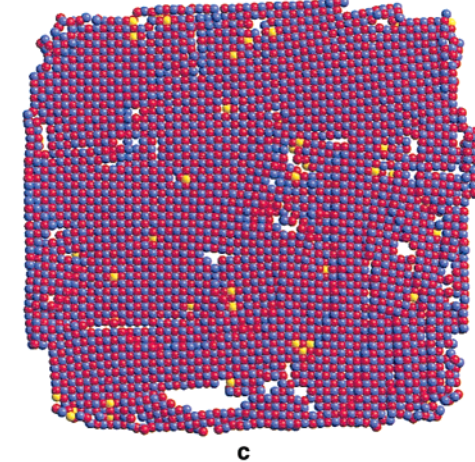
steps are present at the surface. There are no high-angle grain boundaries within the SrO thin film in contrast to the nanoparticle; rather the SrO exists as a single, albeit defective, crystal.

**Interfacial Regions.  $\text{CaO}/\text{MgO}(001)$ .** The position of ions present within the interfacial MgO(002), CaO(002), and penultimate interfacial CaO(002) planes are presented graphically in Figure 6a–c. The interfacial MgO(002) plane comprises many calcium ions that have migrated from the overlying CaO nanoparticle and which occupy magnesium lattice positions. Specifically, 32% (416 ions) of the magnesium ions have been displaced. This value is calculated based upon the area of the MgO(001) substrate covered by the CaO nanoparticle. Small clusters (or voids) of magnesium and oxygen vacancies are also apparent within the interfacial MgO(002) plane.

The magnesium ions, which have been displaced from the interfacial MgO(002) plane, are evident within the CaO(002) plane of the nanoparticle (Figure 6b) and occupy calcium lattice positions as clusters at both the perimeter and within the body of the nanoparticle. The interfacial CaO(002) plane comprises many voids.

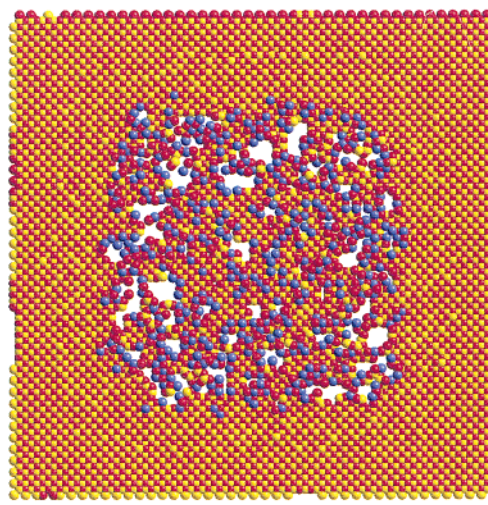
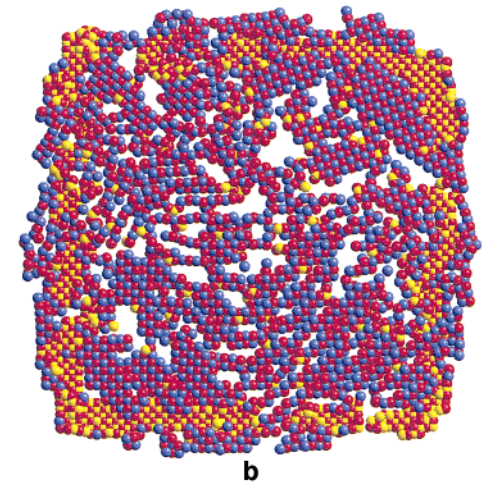
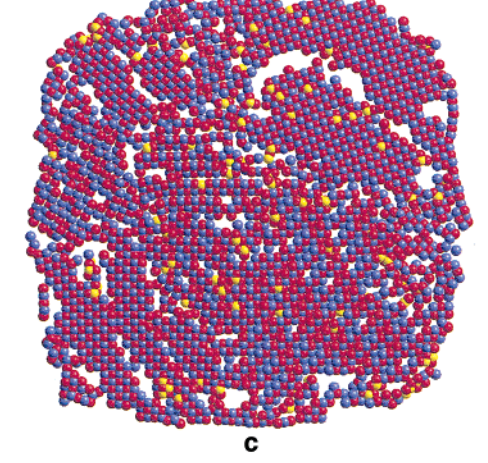
As one traverses to the next interfacial CaO(002) plane, almost full densification of the nanoparticle is observed (Figure 6c), although the plane comprises several oxygen and calcium vacancies. It is also apparent that the nanoparticle exhibits a square cross section, although slight rounding of the corners, via steps and ionic relaxation, is evident.

**$\text{SrO}/\text{MgO}(001)$ .** The positions of ions present within the interfacial MgO(002), SrO(002), and penultimate interfacial SrO(002) planes are presented graphically in Figure 7a–c. In contrast to the CaO nanoparticle, the interfacial MgO(002) plane comprises many more voids, up to about  $100 \text{ \AA}^2$  in size. In addition, there is a high concentration of strontium ions within the interfacial MgO(002) plane, which occupy magnesium lattice sites. Surprisingly, the magnesium ions displaced segregate to the edge of the nanoparticle forming a “strip”, about  $5\text{--}10 \text{ \AA}$  wide, which circumnavigates the interfacial SrO(002) plane of the nanoparticle. We suggest a possible driving force for such a configuration is that the magnesium and oxygen ions comprising the strip maintain registry with the underlying MgO substrate resulting in favorable interfacial interactions. The strontium and oxygen ions enclosed (within the boundaries of this strip) appear at first sight almost amorphous in appearance. However, upon closer inspection, the arrangement of the ions within the

**a****b****c**

**Figure 6.** Plan views of slices, cut parallel with the interfacial plane, through the CaO/MgO(001) nanoparticle system with sphere model representations of the atom positions; (a) interfacial MgO region; (b) interfacial CaO region; (c) penultimate interfacial CaO region. Calcium ions are colored blue, magnesium is yellow, and oxygen is red.

interfacial region arises from the various misaligned crystallites, which comprise the nanoparticle. For example, the ions comprising domains within the top left of Figure 7b appear to be rotated by about  $35^\circ$  about an axis perpendicular to the surface of the MgO(001) substrate. This corresponds to the region, top left, colored gray in Figure 4a. Far right (Figure 7b) the rotational angle is approximately  $15^\circ$  (crystallite colored yellow in Figure 4a). Magnesium ions are also observed within the

**a****b****c**

**Figure 7.** Plan views of slices, cut parallel with the interfacial plane, through the SrO/MgO(001) nanoparticle system with sphere model representations of the atom positions; (a) interfacial MgO region; (b) interfacial SrO region; (c) penultimate interfacial SrO region. Strontium ions are colored blue, magnesium is yellow, and oxygen is red.

SrO(002) interfacial plane, occupying strontium lattice positions within the SrO nanoparticle.

Inspection of a plan view of the penultimate interfacial (002) plane of the SrO nanoparticle (Figure 7c) reveals an almost circular cross section for the nanoparticle. The grains comprising the nanoparticle are evident together with a complex structural array of grain boundaries and grain junctions. The nanoparticle

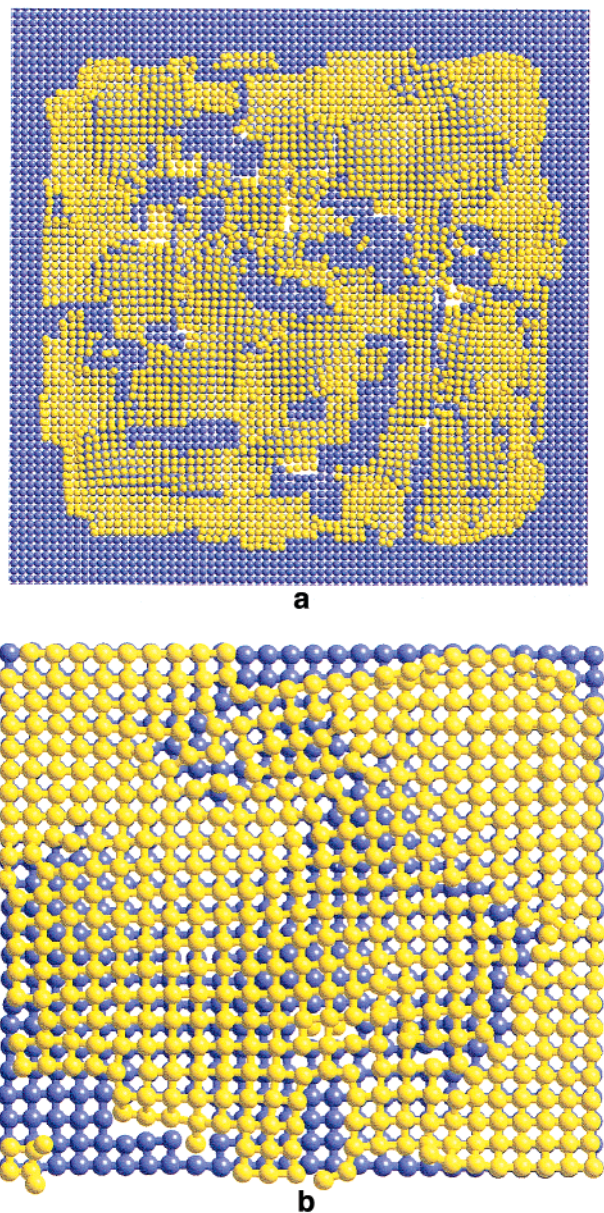


**Figure 8.** Plan views of the interfacial region of the MgO(001) substrate (colored blue) and overlying CaO nanoparticle (colored yellow); (a) full simulation cell; (b) enlarged segment, top right corner of part a depicting more clearly the epitaxial configurations that exist between the nanoparticle and the underlying substrate.

appears to have densified with fewer voids within the layer. In addition, the concentration of magnesium ions, which have migrated from the substrate, are much reduced compared with the interfacial SrO(002) plane.

**Epitaxial Considerations.  $\text{CaO}/\text{MgO}(001)$ .** A plan view of the ions comprising the interfacial CaO nanoparticle and underlying MgO planes is shown in Figure 8a. In Figure 8b, an enlarged segment, taken from the top right-hand corner of Figure 8a, is depicted, which shows more clearly the epitaxial relationships that exist between the CaO and underlying MgO substrate. Specifically, one can observe regions of CaO, which lie commensurate with the underlying MgO and span areas of approximately  $200 \text{ \AA}^2$ ; cations and anions of the overlying CaO lattice lie directly above their respective counterions of the underlying MgO. Connecting regions comprise CaO, which are misaligned with respect to the underlying MgO. Interestingly, at the center and far left of Figure 8b, regions of CaO lie directly

above midpoints between oxygen and magnesium lattice positions of the MgO(001) surface. In addition, dislocations, with mixed screw-edge character, are present and (after careful inspection) are located at regions where the CaO transforms from coherency to regions of misalignment.

A plan view of the interfacial CaO thin film and MgO planes of the supported CaO thin film are depicted in Figure 9a with an enlarged segment (bottom right of Figure 9a) shown in Figure 9b. The thin film displays similar structural characteristics to the nanoparticle with a reduced density of ions at the interfacial region and interconnecting regions of coherency and misalignment. Moreover, there appears to exist some kind of “epitaxial periodicity” with a supercell of  $1200 \text{ \AA}^2$  (Figure 9b) and comprising two large (ca.  $150 \text{ \AA}^2$ ) and two small (ca.  $30 \text{ \AA}^2$ ) coherent circular regions interconnected with misaligned regions. This feature is somewhat different from commensurate relationships, which are observed within lattice misfitting interfacial systems.<sup>15</sup> Specifically, it is not geometrically possible for there to exist two different sized areas of coherence (Figure 9b) for uniformly spaced lattices; rather within this particular system, there must be inhomogeneous spacings between the ions comprising the thin film. The reason for this is linked to the alternating charges of the cations and anions present at the (100) surface of rocksalt materials. In the large areas of coherence, the cation and anions across the interfaces are in close proximity and the CaO is compressed to maintain this registry facilitating more energetically favorable interactions across the interface. As the lattices move out of registry and back again, like ions come into close contact. Here, the CaO expands to limit the length of registry between isovalent ions and results in the smaller regions of registry. This is illustrated by changes in the in-plane distance along a Ca–O chain which transverses both a large and small region. We note that this is the *general* behavior associated with the system, and the explicit atomistic behavior of the ions at these regions is somewhat more complex owing to the presence of defects, dislocations, and ionic relaxation.

**$\text{SrO}/\text{MgO}(001)$ .** A plan view of the interfacial SrO nanoparticle and underlying MgO planes are shown in plan view in Figure 10. In contrast to the CaO nanoparticle, the SrO nanoparticle does not exhibit any discernible regions of coherency, which can be attributed to the nanoparticle comprising various misaligned crystallites, although we note that the MgO “strip”, which surrounds the interfacial SrO layer, lies in registry with respect to the MgO substrate.

In comparison to the SrO nanoparticle, regions of coherency can be observed for the SrO thin film and appear as well ordered circular domains  $20 \text{ \AA}^2$  in area (Figure 11a,b). Regions of coherency for the  $\text{SrO}/\text{MgO}(001)$  are much smaller compared with the  $\text{CaO}/\text{MgO}(001)$  system owing to the much higher lattice misfit associated with the SrO/MgO system. Specifically, the strain energy terms required to bring the SrO into coherence with respect to the MgO substrate are much higher compared with the analogous  $\text{CaO}/\text{MgO}(001)$ . However, a similar, but less pronounced, cycle of large and small domains is also observed.

On the other hand, one might describe the SrO as lying commensurate with respect to the underlying MgO(001). Specifically, one can adjudge in Figure 11(b) regions in which 9 SrO lattice spacings are matched with 11 MgO lattice spacings of the support. Upon the basis of the Sr–O and Mg–O distances for the parent oxides ( $2.58$  and  $2.1 \text{ \AA}$  respectively), the misfit (following eq 2) associated with such a configuration is  $+0.5\%$ , which compares with  $+21\%$  for a coherent configuration.

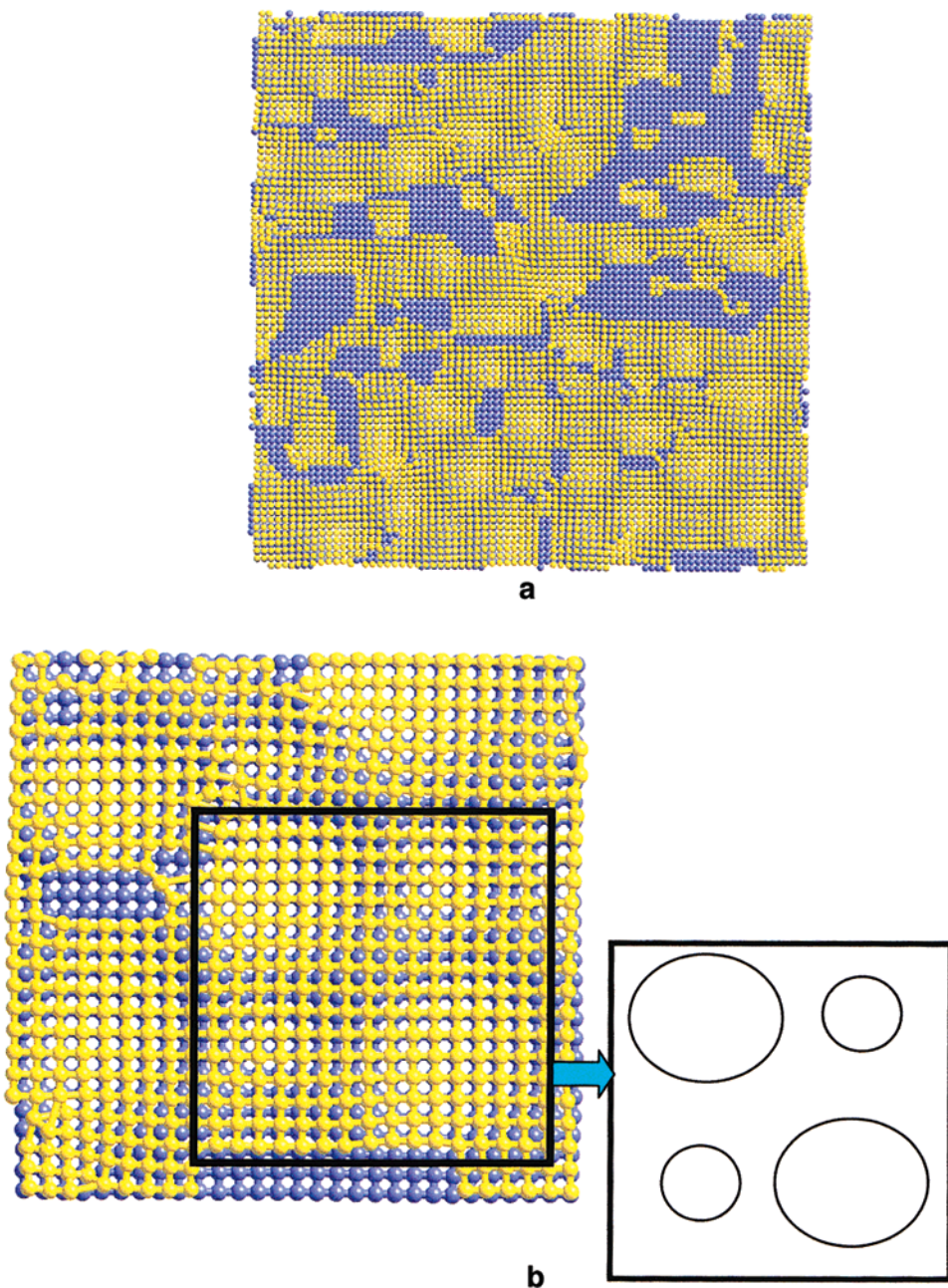


**Figure 9.** Plan views of the interfacial region of the MgO(001) substrate (colored blue) and overlying CaO thin film (colored yellow); (a) full simulation cell; (b) enlarged segment, bottom right corner of part a depicting more clearly the epitaxial configurations that exist between the thin film and the underlying substrate. To the right of part b a schematic is presented illustrating the “four circular regions” of coherence.

Clearly, the strain energy terms required to ensure such a commensurate a relationship is much smaller compared with the energy required to bring the two lattices into coherence. Moreover, that such a configuration has evolved suggests that the reduction in strain outweighs the deleterious influence of bringing like-charged ions into close proximity (misaligned regions). In addition, upon close inspection and measurement of inter-ion distances between like-charged ions, we find that ionic relaxation (and dislocation formation) acts to increase the distance between like-charged ions and thereby help to stabilize the system across the interfacial region.

**Ion Densities.** To help understand further the structure of the supported nanoparticles and thin films, the ion densities of the oxide overlayer and substrate, as a function of distance, were calculated for each system. The ion densities have been calculated using the MDPREP code<sup>32</sup> to indicate any changes in the layers of the rocksalt structured lattices. The ion density,

$z(x)$ , is defined as the number of atoms of a given type, within a given slice (parallel with the surface plane) within the simulation cell, normalized to the average density:

$$z(x) = \frac{V}{NA\delta x} \left\langle \sum_i \delta(x - x_i) \right\rangle \quad (4)$$

where  $V$  is the simulation cell volume,  $N$  is the number of atoms of the given type,  $A$  is the area of the interface,  $x_i$  is the perpendicular height of atom  $i$ , and  $\delta x$  is the histogram width over which the  $\delta$  function gives one. A value of 1.0 thus represents the average density for that species within the entire simulation cell (including the vacuum) with larger values indicating increased density and the formation of well-defined crystal planes. Density traces are presented for the CaO/MgO-(001) nanoparticle, CaO/MgO(001) thin film, SrO/MgO(001)

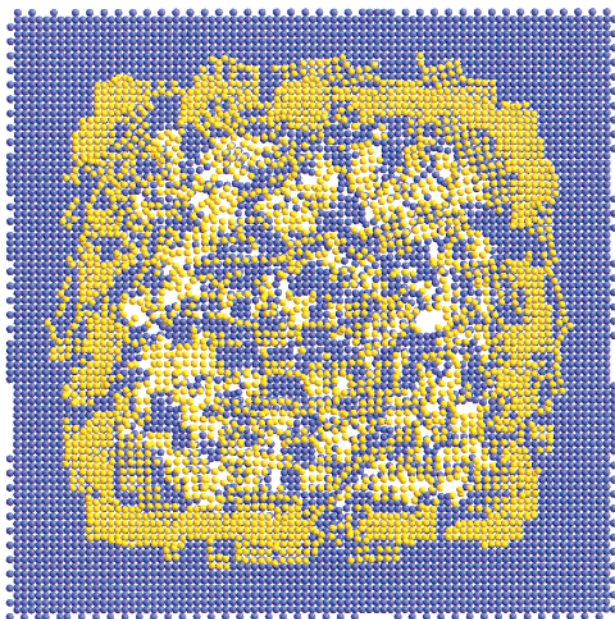
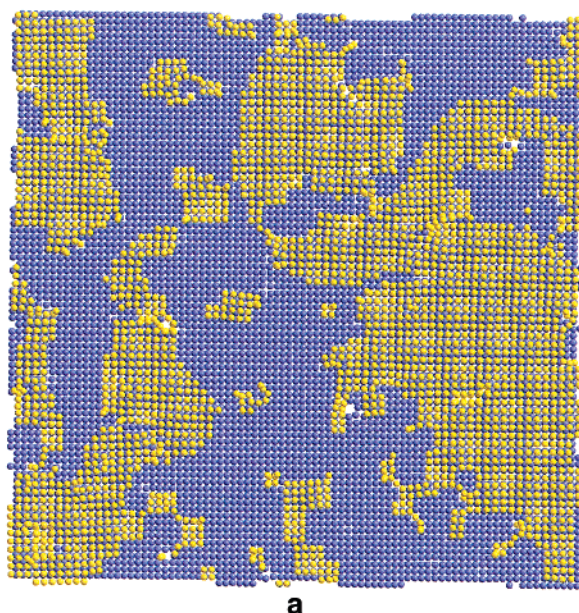


**Figure 10.** Plan view of the interfacial region of the MgO(001) substrate (colored blue) and overlying SrO nanoparticle (colored yellow).

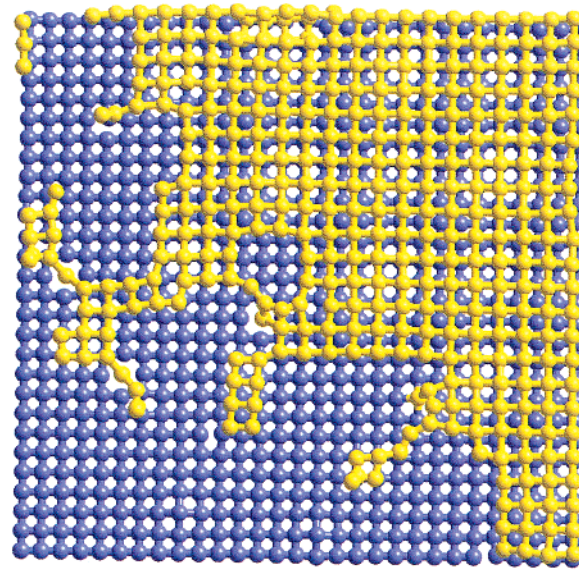
nanoparticle, and SrO/MgO(001) thin film in Figure 12a–d, respectively.

*CaO/MgO(001).* Figure 12a shows the ion densities of both the MgO substrate and overlying CaO nanoparticle within the CaO/MgO(001) system. The bottom of the MgO substrate is located at a depth of 0, with the first six (blue) peaks corresponding to MgO(002) planes. Because these planes are within region II of the simulation cell, the ions are held fixed, and so the peaks are sharp. Conversely, the following two peaks, which relate to the penultimate interfacial and interfacial MgO(002) planes, are allowed to move within the simulation. Consequently, the peaks are broadened, which reflects the response of ions within these two planes to the overlying CaO nanoparticle. The remaining (red) peaks correspond to the overlying CaO nanoparticle, which one can estimate loosely as being about 30 Å thick (measured from the central region of the nanoparticle to the underlying MgO) and comprising 10–12 CaO(002) planes. The peak height diminishes as one proceeds further from the interfacial plane reflecting the convex or droplet morphological structure of the nanoparticle; that is, the planes step up toward the center of the cluster. The red peaks are poorly resolved and broad, indicating considerable perturbation and curvature of the CaO(002) lattice planes and indicating also the presence of the many dislocations within the CaO nanoparticle. The resolution is particularly poor at the interfacial region. This may be attributed to the observed low density of ions within the interfacial region (Figure 8a), which gives rise to increased relaxational freedom and subsequent disorder of the ions in this region.

The CaO–MgO interfacial separation can be estimated from the figure to be about 3.6 Å or about 1.2 Å larger than bulk CaO. We suggest that the high interfacial distance enables the system to maximize interfacial interactions thereby stabilizing the interface; like-charged ions are not constrained to be in close proximity at the interfacial region. Conversely, the trace does not go to zero at the interfacial region indicating that there is a significant density of ions located within this region. Consequently, the definition of the interfacial distance is necessarily rather ambiguous.



a



b

**Figure 11.** Plan views of the interfacial region of the MgO(001) substrate (colored blue) and overlying SrO thin film (colored yellow); (a) full simulation cell; (b) enlarged segment, bottom right corner of part a depicting more clearly the epitaxial configurations that exist between the thin film and the underlying substrate.

The figure also indicates that calcium ions, which have migrated into the interfacial MgO(002) plane, lie about 0.3 Å above the MgO(002) plane; the red (calcium) peak is displaced 0.3 Å to the right of the blue peak corresponding to the interfacial magnesium ions and is consistent with the difference in the lattice constants of MgO and CaO. In addition, the magnesium ions displaced, which occupy regions within the interfacial CaO(002) plane, are 2.05 Å above the interfacial MgO(002) plane or consistent with MgO(002) interplanar distances in the parent MgO. Such observations are consistent with the fact that magnesium ions are smaller compared with calcium. Interatomic CaO(002) distances within the CaO nanoparticle are estimated to be about 2.45 Å. One can also notice that magnesium ions migrate as far as 8 Å into the CaO nanoparticle.

In Figure 12b, the density, as a function of distance, for the CaO/MgO(001) thin-film system is presented. The thin film (ca.

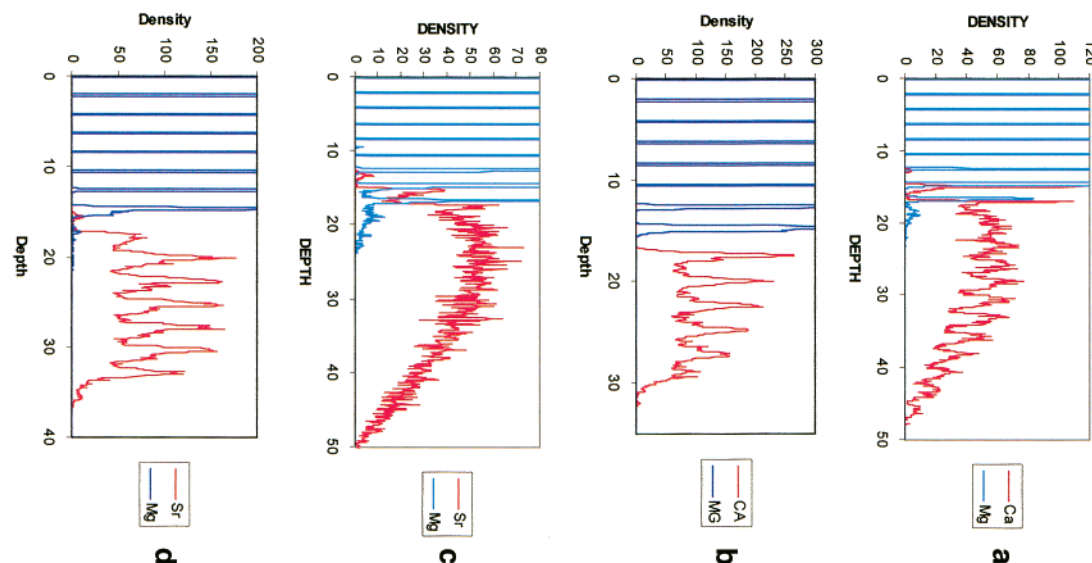


**Figure 12.** Ion densities calculated as a function of distance along the [001] within (a) CaO/MgO(001) nanoparticle; (b) CaO/MgO(001) thin film; (c) SrO/MgO(001) nanoparticle; (d) SrO/MgO(001) thin film. The ionic densities were integrated over a distance of 0.1 Å. The depth is measured in angstroms.

15 Å thick) comprises about 5–6 CaO(002) layers with incomplete filling of the surface. CaO(002) distances are calculated to be about 2.4 Å with an interfacial separation of 2.6 Å, or 1.0 Å lower compared with the interfacial separation of the CaO nanoparticle supported on MgO(001). In contrast to the system comprising a CaO nanoparticle supported on MgO(001), there is little migration of magnesium and calcium ions across the interfacial region, and the peaks corresponding to the calcium ions are more clearly resolved because there is much less distortion of the CaO(002) planes. Some distortion does occur, owing to the evolution of screw-edge dislocations within the CaO lattice; between peaks, the trace does not go to zero. In particular, the atoms comprising the CaO(002) layers spiral up, via screw-edge dislocations, to facilitate continuity with CaO(002) planes above.

*SrO/MgO(001).* From the SrO/MgO(001) density trace (Figure 12c), the SrO nanoparticle can be estimated as being about 34 Å thick (measured from the central region of the cluster to the underlying MgO support). Owing to the many misoriented SrO grains that comprise the nanoparticle, the figure does not exhibit well-defined peaks because the planes within the

**TABLE 1:** Summary of the Structural Features Associated with the MO/MgO(001) Systems (M = Ca, Sr; N = Nanoparticle; TF = Thin-Film) Including the (Bulk) Lattice Misfit (*F*) Associated with Each System, the Morphological Structures, Epitaxial Configurations Associated with the Oxide Overlayer and Substrate, Average Nearest Neighbor Distances, Calculated from the Radial Distributions (RDF), within the Overlying Oxide and Substrate together with the Range over which the Average is Calculated, and Structural Details Pertaining to the Interfacial Region together with the Approximate Interfacial Distance and Defects Identified to Have Evolved within the Supported Oxides

system	<i>F</i>	morphology	epitaxy	RDF	interfacial region	defects
CaO (N)	+13% 4.80 Å	pseudo convex lens, 13 × 13 × 3 nm plane curvature single crystal {001} surfaces exposed	coherency (ca. 200 Å <sup>2</sup> ) misalignment	CaO: 2.33, 2.47 (split peak) (range 2.0–2.7 Å) MgO: 2.08 (range 1.9–2.2 Å)	reduced ionic density (voids) 3.6 Å	screw-edge dislocations isolated and clustered vacancies Ca, Mg substitutionals migration of Mg ca. 8 Å into nanoparticle
CaO (TF)	+13%	thickness: ca. 1.5 nm single crystal CaO(001) surface exposed monatomic, + (occasional) diatomic steps on surface	coherency (circular ca. 150 Å <sup>2</sup> ) misalignment	CaO: 2.35 (range 2.1–2.6) MgO: 2.08 (range 2.05–2.10 Å)	reduced ionic density 2.6 Å	screw-edge dislocations isolated and clustered vacancies Ca, Mg substitutionals
SrO (N)	+21% 5.16 Å	convex lens-type, radius 14–15 nm, height 3.5 nm ten interconnecting misaligned crystallites monatomic (few diatomic) steps on nanoparticle surface {001} surfaces exposed	no coherency	SrO: 2.58 (range 2.2–2.9) MgO: 2.08 (range 2.05–2.10)	reduced ionic density interfacial separation unresolved	grain boundaries grain junctions screw-edge dislocations migration of Mg ca. 9 Å into nanoparticle
SrO (TF)	+21%	thickness: ca. 1.8 nm single crystal SrO(001) surface exposed monatomic, + (occasional) diatomic steps on surface	coherency (circular ca. 20 Å <sup>2</sup> ) misalignment commensurate structure: 9SrO/11MgO (0.5% misfit)	SrO: 2.60 (range 2.3–2.8) MgO: 2.08 (range 2.05–2.10)	3.2 Å	no grain boundaries screw-edge dislocations Sr, Mg substitutionals

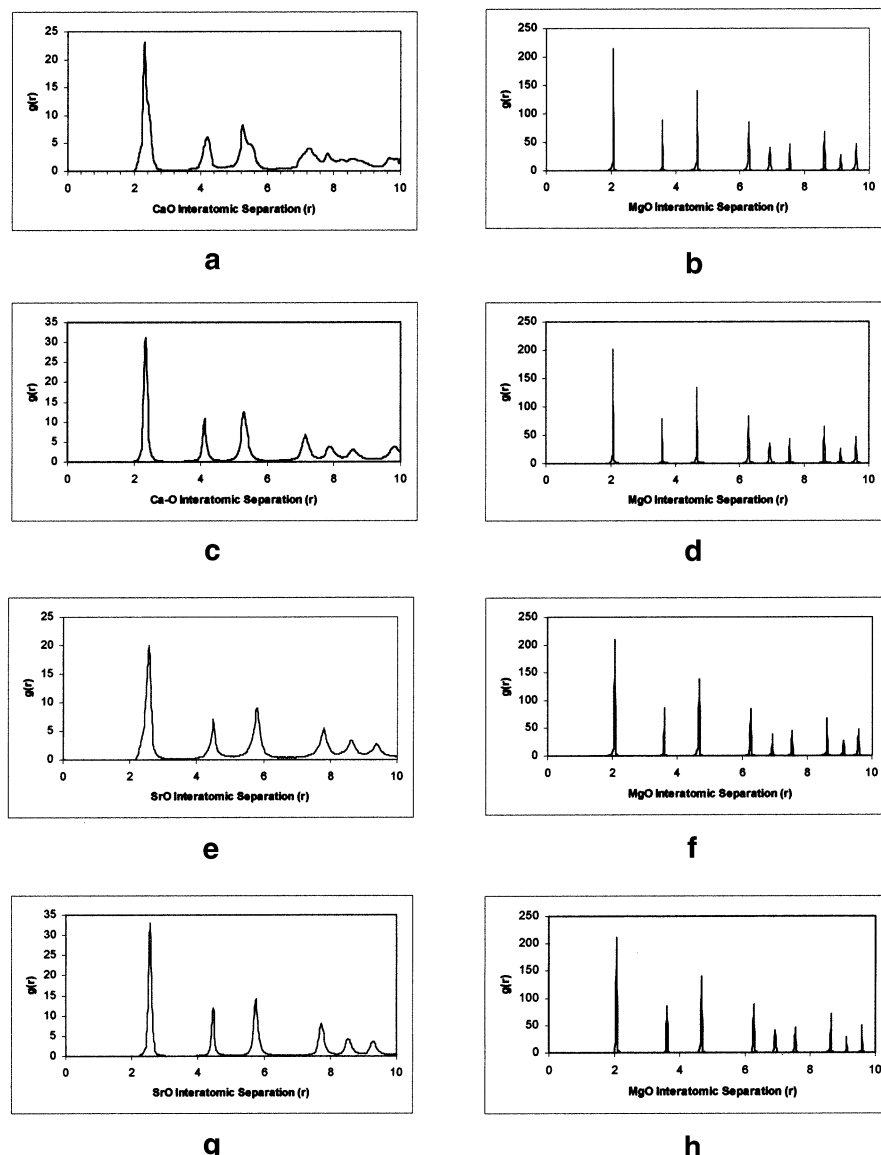


**Figure 13.** Calculated RDF for (a) CaO nanoparticle; (b) MgO substrate (CaO/MgO(001) system); (c) CaO thin film; (d) MgO substrate (CaO/MgO(001) system); (e) SrO nanoparticle; (f) MgO substrate (SrO/MgO(001) system); (g) SrO thin film; (h) MgO substrate (SrO/MgO(001) system). Interatomic separations are measured in angstroms.

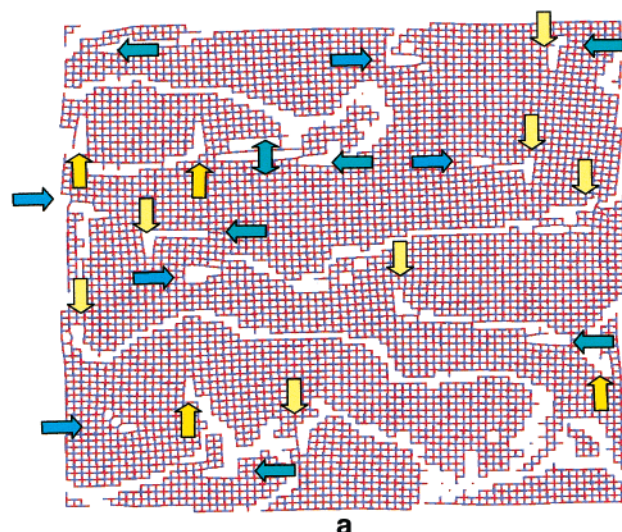
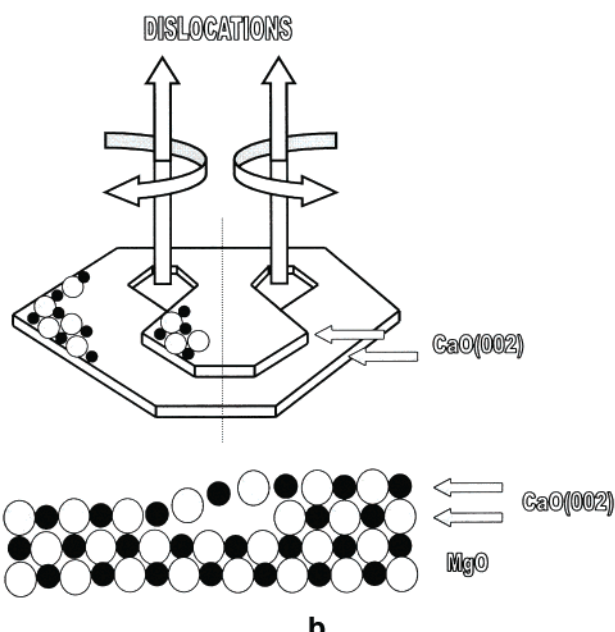
nanoparticle to not lie parallel with the underlying substrate. However, the figure does indicate migration of magnesium ions as far as 9 Å into the SrO with the strontium ions displaced migrating into the interfacial MgO planes. The peaks corresponding to the strontium ions, which have migrated into the support, are displaced about 0.7 Å to the right of the peaks corresponding to magnesium ions in the same layer. This we suggest is because of the larger size of the strontium compared with the magnesium ion, and consequently, the strontium ions lie slightly above the MgO plane. Similar to the CaO/MgO-(001) system, the magnesium peak commensurate with the interfacial SrO(002) peak is high owing to the considerable migration of magnesium ions into the interfacial plane of the nanoparticle and is manifested structurally as a strip enclosing the SrO ions (Figure 7b).

The ion density as a function of distance for the analogous SrO/MgO(001) thin-film system is presented in Figure 12d. The SrO thin film (18 Å thick) comprises about 6–7 SrO(002) layers with interplanar distances of about 2.6 Å with an interfacial separation of about 3.2 Å. The discontinuity between the MgO and overlying SrO at the interfacial region is sharper than the

analogous SrO nanoparticle although there is some migration of cations across the interfacial plane. That the density trace between peaks does not return to zero can again be attributed to the evolution of screw-edge dislocations within the thin film. In addition, the peak corresponding to the interfacial SrO(002) plane is small reflecting the reduced density of ions at the interfacial region.

**Radial Distribution Function (RDF).** Calculated CaO and MgO RDF for each of the four systems are presented in Figure 13a–h for each of the four systems. Calculated nearest neighbor distances for the MO nanoparticle or thin film and underlying MgO substrates are presented in Table 1.

**Structural Features: Dislocations and Grain Boundaries.** Inspection of the ions comprising the various systems (Figures 2–5) reveals little information regarding the various structural features that are present within the material. Accordingly, graphical techniques are required extensively to manipulate the systems to locate and identify the various features. For example, those ions comprising the core of an edge dislocation are characterized by having a lower coordinative saturation. By cutting and inspecting a series of slices within the lattice, through

**a****b**

**Figure 14.** (a) Plan view, with stick model representation of the atom positions, of a thin slice cut parallel to the interfacial plane through the CaO thin film in the CaO/MgO(001) system. The arrows on the figure reveal the complex dislocation network that exists within the thin film by indicating the location of the dislocation cores (the blue and yellow arrows reflect simply dislocations in different directions). The “channels” relate to where part of the CaO lattice moves up and over a neighboring CaO(002) plane; a schematic (b) shows how this is achieved via a screw edge dislocation.

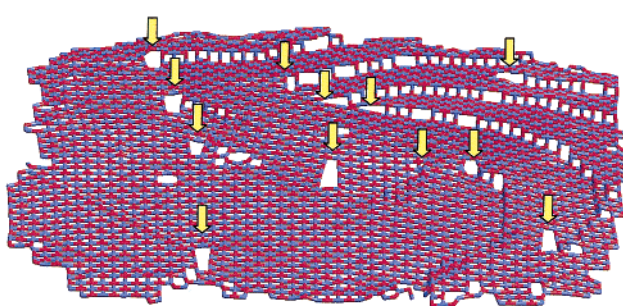


**Figure 15.** Perspective view of a thin slice cut parallel with the interfacial plane through the CaO nanoparticle in the CaO/MgO(001) system. The arrows indicate the location of screw-edge dislocation cores. The figure also demonstrates the spiral nature (right of figure) of the overlap between CaO(002) planes, facilitated via the dislocations.

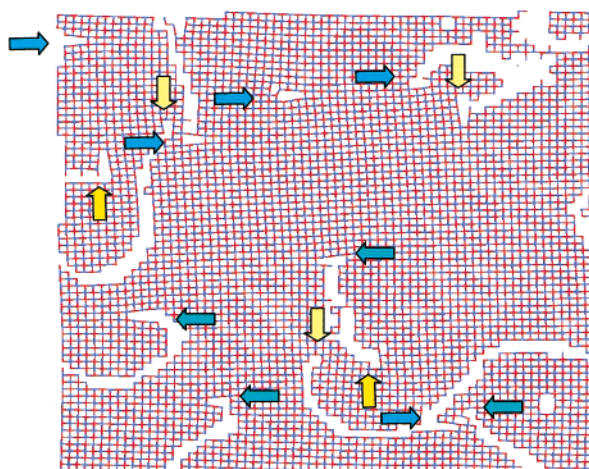


**Figure 16.** Plan view, with stick model notation, of a thin slice cut parallel with the interfacial plane, through the SrO thin film in the SrO/MgO(001) system. The arrows on the figure reveal the complex dislocation network that exists within the thin film by indicating the location of the dislocation cores. The “channels” relate to where part of the SrO lattice moves up and over a neighboring SrO(002) plane.

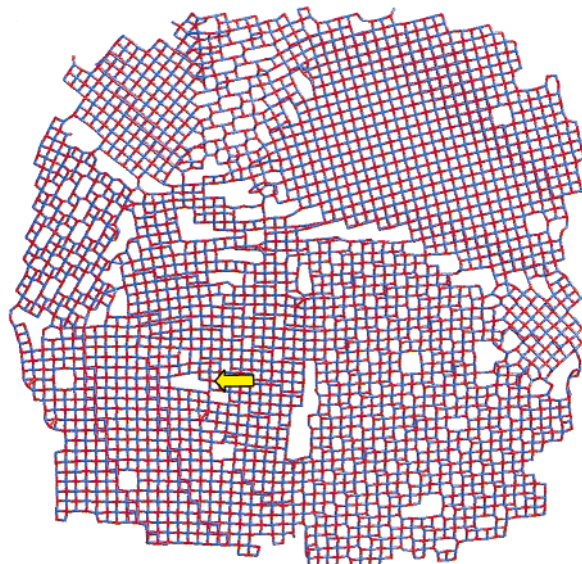


**Figure 17.** Plan view of a thin slice cut parallel with the interfacial plane through the SrO nanoparticle in the SrO/MgO(001) system. The arrow indicates the location of a screw-edge dislocation that has evolved within one of the interconnecting crystallites comprising the nanoparticle.

which the dislocation traverses, the ions within a dislocation core can be labeled and the surrounding lattice removed. Finally, by piecing together all of the ions comprising the dislocation in each slice, a 3D visual representation of the dislocation core is obtained. Similar procedures have been used to ascertain the grain-boundary structures.

**Dislocation Networks.** Figures 14–17 depict thin slices cut parallel with the interfacial plane through the nanoparticles and thin films to show the position and concentrations of the dislocation networks, which have evolved within the supported material.

The locations of edge or mixed screw/edge dislocations are relatively simple to locate for rocksalt-structured oxides (compared with, for example, fluorite structured oxides<sup>33</sup>). Specifically, they are typified by a rhombus rather than a square, with the ion on one side having a coordination number of five rather than six.

**TABLE 2: Summary of the Various Nanoparticle Morphologies, Structural Features, and Epitaxial Relationships as a Function of System Misfit, F**

SCHEMATIC	SYSTEM	F	STRUCTURE	EPI TAXY	REFERENCE
	SrO/MgO(001)	+21%	Grain-boundaries	Intractable	This study
	CaO/MgO(001)	+13%	Dislocations	Coherence 200 Å²	This study
		0%			
	SrO/BaO(001)	-7%	'Perfect crystal' (no dislocations or grain-boundaries)	Full Coherence	[28]
	CaO/BaO(001)	-14%	Dislocations	Coherence 200-300 Å²	[28]
	MgO/BaO(001)	-27%	Grain-Boundaries	Intractable	[21]

*CaO/MgO(001)*. In Figure 14a, a plan view of a CaO slice, cut through the CaO thin film parallel with the interfacial plane, is shown. The arrows depict the position within the lattice where each dislocation core resides. The figure also displays what appear to be channels traversing “randomly” within the plane. These regions correspond to where the lattice moves up and over the CaO(002) plane below and facilitated by a screw-edge dislocation. A schematic to aid interpretation is shown in Figure 14b. The double-headed arrow (center top left) is a region of lattice slip within the CaO.

For the CaO nanoparticle, supported on MgO(001), a perspective view of the slice is depicted in Figure 15. Similar to the CaO thin film, the nanoparticle comprises a complex dislocation network. Interestingly, where the CaO(002) planes overlay underlying (002) planes (facilitated by screw-edge dislocations), the lattice appears to spiral. Moreover, there appears to be some kind of regularity associated with the (002) planes moving over one another within the nanoparticle in contrast to the thin film, which appears random. We suggest that this is because of the lens-type morphology of the nanoparticle. Specifically, the (002) planes exhibit curvature from the center of the nanoparticle to the edges (lens-type morphology).

*SrO/MgO(001)*. An analogous slice is depicted in Figure 16 for the SrO/MgO(001) thin film. For this system, there is a lower concentration of dislocations and associated channels corresponding to the moving of one SrO(002) plane over the (002) plane below.

For the SrO nanoparticle supported on MgO(001), the structure of the slice (Figure 17) is somewhat more complex owing to the misoriented crystallites, which comprise the nanoparticle. Whereas some crystallites are oriented with (002) planes parallel with respect to the underlying MgO(001) (top right, top left, and bottom left, although the latter is vicinal), others are not, and therefore, the regular square lattice is obscured within a plan view. However, one can observe various

grain-boundary structures, which appear similar to those seen experimentally in NiO.<sup>34</sup>

**Dislocation Cores.** We now consider the core structures of a few dislocations within (for reasons of illustration) the CaO nanoparticle.

Figure 18a depicts the core structure of four interconnecting screw-edge dislocations. The dislocations traverse the entire thickness of the CaO nanoparticle and lie at about 45° to the surface normal. The dislocations are pinned at the center.

All of the dislocations are of mixed screw-edge character and are symmetrically equivalent. The Burgers vector of the dislocation, colored green, is  $\frac{1}{2}[011]$ , with screw component  $\frac{1}{2}[001]$  and edge component  $\frac{1}{2}[010]$ . The other dislocations are rotated, about the [001], with Burgers vectors of  $\frac{1}{2}[011]$  (blue),  $\frac{1}{2}[101]$  (red), and  $\frac{1}{2}[101]$  (grey). In addition, there is a further dislocation colored yellow in Figure 18b, with Burgers vector  $\frac{1}{2}[011]$  and which intersects the blue dislocation at the central part. Indeed, the blue and yellow dislocations “share” part of their cores. Moreover, at the central region, the edge components of the yellow ( $\frac{1}{2}[010]$ ) and blue ( $\frac{1}{2}[0\bar{1}0]$ ) dislocations appear to have annihilated. Clearly, the dislocation network within the nanoparticle is highly complex.

**Grain-Boundaries.** A grain-boundary (GB) may be considered as two connecting surfaces, where the crystals comprising each surface are misaligned. If the axis of rotation is parallel with the interfacial plane between the two crystals, the boundary can be classified as a “tilt-boundary”. Conversely, if the axis of rotation is perpendicular, a twist boundary results. A general boundary is a combination of the two.<sup>15</sup> It is also well-known that, for misorientation (tilt) angles of <15°, the GB comprises an array of dislocations (low angle GB). However, as the misorientational angle increases beyond 15°, the dislocation cores overlap and a somewhat different structure appears (high angle GB).<sup>17</sup> For the SrO nanoparticle supported on MgO(001), various general grain-boundaries are formed between the various crystallites comprising the nanoparticle. Moreover, owing to the

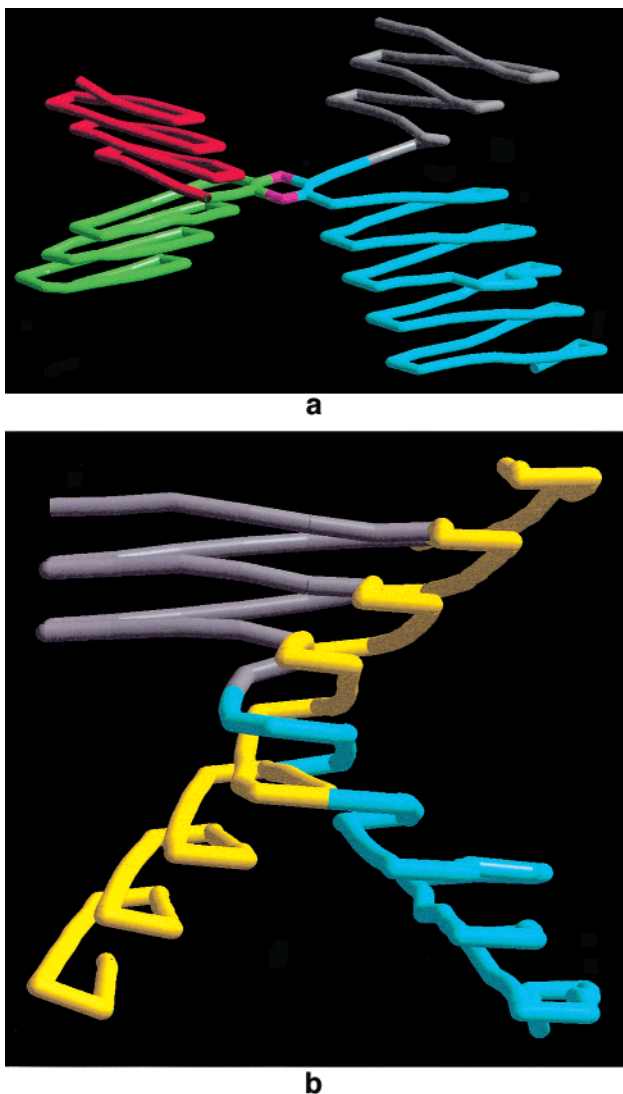


**Figure 18.** (a) Stick model representation of the spiral of atoms comprising the core structure of four interconnecting screw-edge dislocations. (b) Depicts an additional screw-edge dislocation (colored yellow), which traverses through the intersection of the four dislocations shown in part a. To improve clarity of part b, the two dislocations colored red and green have been omitted.

curvature of the lattice planes comprising the various crystallites within the SrO nanoparticle, assigning various indices to describe the GB and classifying the boundary as either tilt, twist or general has proved difficult and perhaps misleading as the index will inevitably change as one traverses along the boundary plane. Accordingly, we have employed visualization techniques to show the various GB within the SrO nanoparticle (Figure 17).

However, one particular region, shown in Figure 19, can perhaps be classified as a (410) tilt-boundary with an associated 28° angle between the two lattices. Such a structure is similar to those observed experimentally in NiO and studied theoretically.<sup>19,34</sup> However, for this particular GB, the calculated angle is only about 20°, which may be a consequence of the GB terminating at the surface of the nanoparticle (the surface is at the top of the figure).

A summary of the structural features associated with the CaO/MgO(001) and SrO/MgO(001) systems is presented in Table 1.

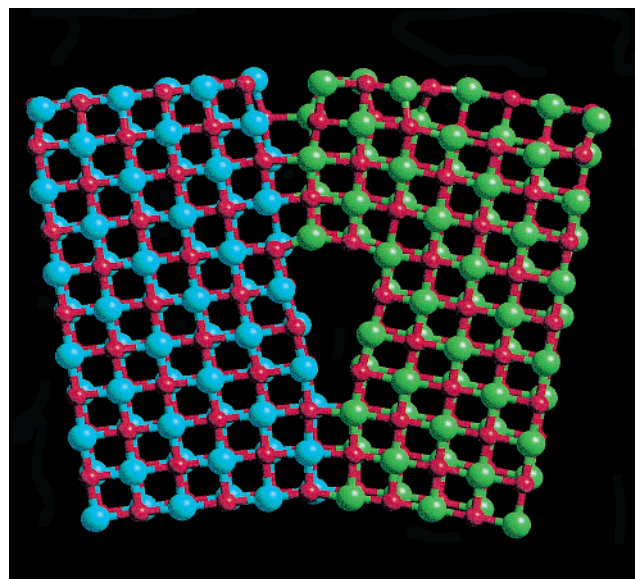


**Figure 19.** Ball and stick model representation of a segment of the SrO nanoparticle (shown in Figure 4) showing more clearly the grain-boundary structure between two interconnecting and misaligned SrO grains. Strontium is colored blue and green, and oxygen is red. The surface of the nanoparticle is the top of the figure.

## Discussion

Together with previous findings,<sup>21,28</sup> we now compare the influence of the lattice misfit associated with the system (nanoparticle and substrate) on the morphological appearance and structure of the nanoparticles (Table 2).

For high negative lattice misfits, for example the MgO/BaO-(001) ( $F = -27\%$ ) system, the simulations suggest that the nanoparticle comprises many interconnecting crystallites resulting in a concave-lens-type morphological appearance.<sup>21</sup> Conversely, for high positive misfits, SrO/MgO(001) ( $F = +21\%$ ), the simulations predict a convex or droplet morphology. Again, the nanoparticle comprises many misoriented and interconnecting crystallites, which give rise to a complex network of grain boundaries and grain junctions.

As the misfit associated with the system is reduced, so the “curvature” of the nanoparticle diminishes. For these systems, the nanoparticles exhibit slab morphologies. In addition, these “low-misfit” systems exhibit regions of coherence between the nanoparticle and underlying substrate. Indeed, for the SrO/BaO-(001) ( $F = -7\%$ ) system the SrO nanoparticle was observed to be completely coherent with respect to the substrate and comprised no dislocations; nanoparticles can be made superhard owing to the lack of dislocations within the material or superplastic due to the large number of grain boundaries.<sup>35</sup>

Nanoparticulate MgO has also been shown to be a far better adsorber of pollutant gases than bulk MgO, which cannot be attributed to a simple increase in the ratio of surface area to volume. It has been suggested (with supporting AFM data<sup>36</sup>) that the faces of the nanoparticles are not {100}, as are bulk crystals; rather higher index and therefore potentially more reactive surfaces are exposed. Experimentally, although STM images of nanoparticles are becoming more common, it is difficult to establish the detailed atomistic structure of the various surfaces.

The structures derived in this study can help explain these experimental findings. For example, for the MgO/BaO system, the MgO exposes the (111) plane at the interface; specifically, MgO(111)/BaO(001). Consequently, the various exposed facets

do not comprise simply {100} surfaces; rather a complex arrangement of mono-, di-, and tri-atomic steps are observed and may prove more reactive compared with a (more stable) {100} face.

In addition, the bending of the crystal planes (droplet morphology) within the CaO and SrO nanoparticles, supported on MgO(001) and the presence of grain-boundaries and grain-junctions (SrO/MgO) leads to changes in bond distances and coordination numbers at the surface of these nanoparticles; the surfaces cannot be defined as simply {100} and may exhibit markedly changed reactivities.

## Conclusion

We have shown that by employing an amorphization and recrystallization strategy, models for oxide nanoparticles supported on an oxide substrate can be generated. The resulting models comprise structural features expected within a supported oxide. These include morphological appearance, surface facets and structure, epitaxial configurations, reduced interfacial ion densities, grain boundaries, grain junctions, dislocation networks, vacancies, substitutionals, interstitials, and defect clusters. An examination of the morphological changes of these clusters as a function of lattice misfit reveals systematic changes: Large positive misfits give rise to convex nanoparticles, whereas large negative lattice misfits give rise to concave nanoparticles. Low misfits are associated with slab morphologies and give rise to coherence between the support and nanoparticle. Such models will be useful in helping to explain the remarkable structures and properties of nanoparticles compared with the parent materials.

Future studies will be performed using a shell model representation of the ions to explore the influence of polarization on the structures of supported nanoparticles. A preliminary study can be found in ref 37.

**Acknowledgment.** We acknowledge funding for a 20 processor Compaq SC cluster, located at the Rutherford Appleton Laboratory, which was purchased and supported with funding from the JREI (JR99BAPAEQ) and Compaq. G.W.W. thanks Enterprise Ireland for a Basic Research Grant (SC/2001/233).

## References and Notes

- (1) Gleiter, H. *Acta Mater.* **2001**, *48*, 1.
- (2) Sayle, D. C.; Watson, G. W. *J. Mater. Chem.* **2000**, *10*, 2241.

- (3) Jia, C. L.; Siegert, M.; Urban, K. *Acta Mater.* **2001**, *49*, 2783.
- (4) Ernst, F.; Recnik, A.; Langjahr, P. A.; Nellist, P. D.; Ruhle, M. *Acta Mater.* **1999**, *47*, 183.
- (5) Sayle, D. C.; Watson, G. W. *Surf. Sci.* **2001**, *473*, 97.
- (6) Sayle, D. C.; Watson, G. W. *Phys. Chem. Chem. Phys.* **2000**, *2*, 5491.
- (7) Chambers, S. A. *Surf. Sci. Rep.* **2000**, *39*, 105.
- (8) Tasker, P. W.; Stoneham, A. M. *J. Chem. Phys.* **1987**, *84*, 149.
- (9) Wang, A.; Belot, J. A.; Marks, T. J.; Markworth, P. R.; Chang, R. P. H.; Chudzik, M. P.; Kannewurf, C. R. *Physica C* **1999**, *320*, 154.
- (10) LeGoues, F. K. *Philos. Mag. B* **1988**, *57*, 167.
- (11) Boaro, M.; Trovarelli, A.; Hwang, J.; Mason, T. O. *Solid State Ionics* **2002**, *147*, 85.
- (12) O'Brien, S.; Brus, L.; Murray, C. B. *J. Am. Chem. Soc.* **2001**, *123*, 12085.
- (13) Frenkel, A. I.; Hills, C. W.; Nuzzo, R. G. *J. Phys. Chem. B* **2001**, *105*, 12689.
- (14) Yacaman, M. J.; Ascencio, J. A.; Liu, H. B.; Gardea-Torresdey, J. *J. Vac. Sci., Technol. B* **2001**, *19*, 1091.
- (15) Sutton, A. P.; Balluffi, R. W. *Interfaces in Crystalline materials*; Oxford University Press, Inc.: New York, 1995. Monographs on the physics and chemistry of materials, Vol. 51.
- (16) Khan, M. I. *J. Solid State Chem.* **2000**, *152*, 105.
- (17) Phillpot, S. R.; Kebinski, P. D.; Wolf, D.; Cleri, F. *Interface Sci.* **1999**, *7*, 15.
- (18) Watson, G. W.; Oliver, P. M.; Parker, S. C. *Surf. Sci.* **2001**, *474*, L185.
- (19) Harris, D. J.; Harding, J. H.; Watson, G. W. *Acta Mater.* **2000**, *48*, 3039.
- (20) Sayle, T. X. T.; Catlow, C. R. A.; Sayle, D. C.; Parker, S. C.; Harding, J. H. *Philos. Mag.* **1993**, *A68*, 565.
- (21) Sayle, D. C.; Watson, G. W. *J. Phys. Chem. B* **2002**, *106*, 3916.
- (22) Sayle, D. C.; Watson, G. W. *J. Phys. Chem. B* **2001**, *105*, 5506.
- (23) Maicaneanu, S. A.; Sayle, D. C.; Watson, G. W. *J. Phys. Chem. B* **2001**, *105*, 12481.
- (24) Sutton, A. P.; Balluffi, R. W. *Acta Metal.* **1987**, *35*, 2177.
- (25) Sayle, D. C. *J. Mater. Chem.* **1999**, *9*, 2961.
- (26) Sayle, D. C.; Catlow, C. R. A.; Dulamita, N.; Healy, M. J. F.; Maicaneanu, S. A.; Slater, B.; Watson, G. W. *Mol. Simul.* **2002**, *28*, 683.
- (27) Baker, J.; Lindgard, P.-A. *Phys. Rev. B* **1999**, *60*, 16941.
- (28) Sayle, D. C.; Watson, G. W. *Phys. Rev. B* **2002**, *65*, 245414-1-15.
- (29) Lewis, G. V.; Catlow, C. R. A. *J. Phys. C: Solid State Phys.* **1985**, *18*, 1149.
- (30) Smith, W.; Forester, T. R. *The DL\_POLY Molecular Simulation Package*; URL: [http://www.dl.ac.uk/TCSC/Software/DL\\_POLY](http://www.dl.ac.uk/TCSC/Software/DL_POLY).
- (31) Watson, G. W.; Kelsey, E. T.; DeLeeuw, N. H.; Harris, D. J.; Parker, S. C. *J. Chem. Soc., Faraday Trans.* **1996**, *92*, 433.
- (32) Watson, G. W. *MDPREP*; A computer program for the preparation and analysis of molecular dynamics simulations, 2002. E-mail: watsong@tcd.ie.
- (33) Maicaneanu, S. A.; Sayle, D. C.; Watson, G. W. *Chem. Commun.* **2001**, 289.
- (34) Merkle, K. L.; Smith, D. J. *Phys. Rev. Lett.* **1987**, *59*, 2887.
- (35) Schiotz, J.; DiTolla, F. D.; Jacobsen, K. W. *Nature* **1998**, *391*, 561.
- (36) Stark, J. V.; Park, D. G.; Lagadic, I.; Klabunde, K. J. *Chem. Mater.* **1996**, *8*, 1904.
- (37) Sayle, D. C.; Maicaneanu, S. A.; Watson, G. W. *Phys. Chem. Chem. Phys.*, in press.